The Astrophysical Journal Supplement Series, 223:25 (13pp), 2016 April doi:10.3847/0067-0049/223/2/25

INTERSTELLAR NEUTRAL HELIUM IN THE HELIOSPHERE FROM *IBEX* OBSERVATIONS. IV. FLOW VECTOR, MACH NUMBER, AND ABUNDANCE OF THE WARM BREEZE

Marzena A. Kubiak[1], P. Swaczyna[1], M. Bzowski[1], J. M. Sokół[1], S. A. Fuselier[2,3], A. Galli[4], D. Heirtzler[5], H. Kucharek[5], T. W. Leonard[5], D. J. McComas[2,3], E. Möbius[5], J. Park[5], N. A. Schwadron[5], and P. Wurz[4]
[1] Space Research Centre of the Polish Academy of Sciences (CBK PAN), 00-716 Warsaw, Poland; mkubiak@cbk.waw.pl
[2] Southwest Research Institute, San Antonio, TX, USA
[3] University of Texas at San Antonio, San Antonio, TX, USA
[4] Physikalisches Institut, Universität Bern, Bern, Switzerland
[5] Space Science Center and Department of Physics, University of New Hampshire, Durham, NH, USA
Received 2015 December 22; accepted 2016 March 4; published 2016 April 14

ABSTRACT

Following the high-precision determination of the velocity vector and temperature of the pristine interstellar neutral (ISN) He via a coordinated analysis summarized by McComas et al., we analyzed the *Interstellar Boundary Explorer* (*IBEX*) observations of neutral He left out from this analysis. These observations were collected during the ISN observation seasons 2010–2014 and cover the region in the Earth's orbit where the Warm Breeze (WB) persists. We used the same simulation model and a parameter fitting method very similar to that used for the analysis of ISN He. We approximated the parent population of the WB in front of the heliosphere with a homogeneous Maxwell–Boltzmann distribution function and found a temperature of ~9500 K, an inflow speed of 11.3 km s^{-1}, and an inflow longitude and latitude in the J2000 ecliptic coordinates 251.°6, 12.°0. The abundance of the WB relative to ISN He is 5.7% and the Mach number is 1.97. The newly determined inflow direction of the WB, the inflow directions of ISN H and ISN He, and the direction to the center of the *IBEX* Ribbon are almost perfectly co-planar, and this plane coincides within relatively narrow statistical uncertainties with the plane fitted only to the inflow directions of ISN He, ISN H, and the WB. This co-planarity lends support to the hypothesis that the WB is the secondary population of ISN He and that the center of the Ribbon coincides with the direction of the local interstellar magnetic field (ISMF). The common plane for the direction of the inflow of ISN gas, ISN H, the WB, and the local ISMF is given by the normal direction: ecliptic longitude 349.°7 ± 0.°6 and latitude 35.°7 ± 0.6 in the J2000 coordinates, with a correlation coefficient of 0.85.

Key words: ISM: atoms – ISM: kinematics and dynamics – local interstellar matter – solar neighborhood – Sun: heliosphere

1. INTRODUCTION

Observations of neutral gas by the *Interstellar Boundary Explorer* (*IBEX*; McComas et al. 2009b) provide important insight into the physical state of and processes operating in the interstellar matter in front of the heliosphere. So far, *IBEX* has observed interstellar hydrogen, helium, oxygen, neon, and deuterium (Möbius et al. 2009a; Bochsler et al. 2012; Saul et al. 2012; Rodríguez Moreno et al. 2013; Park et al. 2014, 2015).

Based on *IBEX* observations, Kubiak et al. (2014) discovered a previously unknown population of neutral helium in the heliosphere, which they dubbed the Warm Breeze (WB). This population is most visible in the portion of Earth's orbit just before the region where interstellar neutral helium (ISN He) is observed. Based on the analysis of data collected by *IBEX* over a single season of ISN gas observations, they reported that the source of the WB can be reasonably approximated by a homogeneous Maxwell–Boltzmann population of neutral He gas in a region ~150 au in front of the heliosphere, and they determined the best-fitting temperature $T_{\rm WB}$, inflow direction (ecliptic longitude $\lambda_{\rm WB}$ and latitude $\beta_{\rm WB}$), speed $v_{\rm WB}$, and abundance $\xi_{\rm WB}$ relative to the primary ISN He within relatively broad uncertainties: $\lambda_{\rm WB} = 240^\circ \pm 10^\circ$, $\beta_{\rm WB} = 11^\circ{}^{+7^\circ}_{-3^\circ}$, $v_{\rm WB} = 11 \pm 4$ km s^{-1}, $T_{\rm WB} = 15{,}000^{+6000}_{-8000}$ K, and $\xi_{\rm WB} = 0.07 \pm 0.03$. They also pointed out that the fit quality obtained was not satisfactory, as indicated by a large reduced χ^2 value of ~4, and reported that the signal for some *IBEX* spin angles depended heavily on a hypothetical threshold in the sensitivity of the *IBEX*-Lo instrument to low-energy neutral He atoms.

One of the most important conclusions suggested by Kubiak et al. (2014) is that the WB may be the secondary population of the ISN He gas. The secondary population of heliospheric neutrals is created in the outer heliosheath where the originally unperturbed flow of interstellar plasma is deflected to flow past the heliopause, which is an impenetrable obstacle for interstellar plasma ions. On the other hand, the neutral component of ISN gas is collisionless on spatial scales comparable to the size of the heliosphere and is not subject to the electromagnetic forces governing the plasma, and so it continues its bulk motion almost without modifications. This causes decoupling of the ionized and neutral component flows. The ionized component is compressed and heated while flowing past the heliosphere, which enhances charge-exchange collisions between the perturbed plasma and pristine neutral flows. As a result, some ions that belonged to interstellar plasma become neutralized, and some atoms from the neutral component become ionized and picked up by the plasma flow. Since resonant charge-exchange reactions operate practically without momentum exchange between the collision partners, the new population of neutralized interstellar ions inherits the local parameters of the ambient plasma, which are different from the parameters of the unperturbed interstellar gas, and continue flowing away from their birth location, decoupled from the parent plasma. Some of those atoms enter the

heliosphere where they are subject to gravitational acceleration and ionization. Since the ionization losses in He atoms are relatively small (Bzowski et al. 2013), an appreciable fraction of the secondary He atoms penetrate into Earth's orbit, where they are measured by *IBEX*.

This mechanism of creation of the heliospheric secondary neutral population has been anticipated theoretically for quite a while (Baranov et al. 1981; Baranov & Malama 1993). The secondary population of ISN H has been believed to exist based on many observations carried out using various techniques (see Katushkina et al. 2015 for a recent review), but—to our knowledge—has not previously been unambiguously resolved from the primary population. The secondary He population had been believed to be of negligible abundance (Müller & Zank 2004) because the reaction assumed to be responsible for its creation, $He^+ + H \rightarrow He + H^+$, has a very low cross-section (Barnett et al. 1990), in contrast to similar interactions with oxygen ions. However, Bzowski et al. (2012) pointed out that the cross-section for the charge-exchange reaction between neutral He atoms and He^+ ions is comparable to the large cross-section for the charge exchange between H atoms and protons, and because of the relatively high abundance of He^+ ions in the interstellar gas near the heliosphere (Frisch & Slavin 2003), appreciable amounts of the secondary He atoms should be produced in the outer heliosheath.

If the WB is indeed the secondary population of ISN He, then it provides information about the physical state of interstellar matter in the outer heliosheath because it can be clearly separated from the primary population. Based on an analysis of the secondary population, one can infer the temperature, flow speed, and deflection angle of the flow direction of the secondary component due to the deformation of the heliosphere from axial symmetry by the action of the interstellar magnetic field (ISMF). It was suggested by Lallement et al. (2005) and found from different heliospheric models (e.g., Izmodenov et al. 2005; Pogorelov et al. 2008) that the secondary population of heliospheric neutrals should have a flow velocity vector in the plane formed by the inflow direction of the unperturbed interstellar matter and the unperturbed vector of the ISMF. Thus, if we are able to determine the inflow direction of the secondary component of the ISN gas, then, with the inflow vector of the unperturbed interstellar gas available (Witte 2004; Bzowski et al. 2014, 2015; Leonard et al. 2015; McComas et al. 2015a, 2015b; Schwadron et al. 2015a; Wood et al. 2015), we can also determine the plane in which the ISMF vector is expected to be. Constraining the ISMF vector reduces the number of unknown parameters which hamper heliospheric studies using large simulation codes, like the Moscow Monte Carlo model (Izmodenov & Alexashov 2015), the Huntsville model (Pogorelov et al. 2009), or the University Michigan/Boston University model (Opher et al. 2006).

If, on the other hand, the WB is not the secondary population of ISN He, then an even more compelling question arises: what is its nature and origin? Answering these questions is only possible through a more thorough analysis of the available data, which is the topic of this article. We analyze the WB observations carried out by *IBEX* during the ISN observation seasons from 2010 through 2014 and derive its temperature, abundance, and inflow velocity vector. Based on those parameters and their relation to other heliospheric observables, we discuss possible sources for this population.

2. OBSERVATIONS AND DATA SELECTION

The strategy of ISN observations by *IBEX* has been presented by Möbius et al. (2009b, 2012, 2015b). The details which are most relevant for the present analysis are discussed in Section 2 in Swaczyna et al. (2015); here, we only point out the most important aspects.

IBEX is a Sun-pointing, spinning spacecraft (McComas et al. 2009b) on a highly elongated elliptical orbit around the Earth (McComas et al. 2011), and the *IBEX*-Lo time-of-flight mass spectrometer, used for the ISN atom observations (Fuselier et al. 2009), scans a great circle on the sky perpendicular to the spin axis. The instrument has eight logarithmically spaced energy channels of wide acceptance ($\Delta E/E \simeq 0.7$), which are sequentially switched during operation. ISN atoms are observed over intervals of a few months around the beginning of each calendar year when the spacecraft, together with the Earth, move toward the ISN flow, thus increasing the relative speed (and energy) of the atoms and consequently their flux and the efficiency of their detection. As a result of this observation geometry, the relative energy of neutral He atoms varies during the observation season and also as a function of the spacecraft spin angle. Neutral atoms enter the instrument through a collimator and hit a specially prepared carbon conversion surface, which retains a very thin layer of absorbed material which is mostly water. Some of the species measured by *IBEX*-Lo can be identified directly because upon hitting the conversion surface they form negative ions, which are then extracted by an electric field, accelerated, and analyzed by the electrostatic analyzer. Noble gases like He and Ne, however, do not form stable negative ions, and therefore can be observed only indirectly. When these neutrals hit the conversion surface, they sputter a cloud of negative C, O, and H ions (Wurz et al. 2008), which are collected by the electrostatic analyzer and registered by the time-of-flight spectrometer. Species identification is carried out on the ground through analysis of the proportions between the time-of-flight signals of the sputtered C, H, and O atoms. Details of the measurement process and data flow are presented by Möbius et al. (2015b, 2015a) and details of the species identification by Park et al. (2014, 2015). The sputtering products have energies lower than the energy of the incident atom. The energy spectrum of the sputtering products is relatively flat between 0 eV and a drop off at an energy a little lower than the energy of the incoming neutral atom. In addition, there is a finite minimum energy for an incoming atom to sputter, which we refer to as the energy threshold for sputtering. Therefore, the sputtering products are registered in all of the energy channels between the lowest channel and the channel with the energy acceptance corresponding to the energy of the incoming atom. The most abundant species among the sputtering products of He is hydrogen. H ions sputtered by He are observed mostly in *IBEX*-Lo energy channels 1 through 3. Without further analysis of the proportions of the H^- signal to the signal from the simultaneously registered C^- and O^- ions, the H^- ions sputtered by incident He atoms are indistinguishable from those produced by the incoming H atoms.

The WB is most visible from mid-November to the end of January each year. In this portion of the Earth's orbit, the WB signal observed by *IBEX* is affected by the primary population of ISN He relatively little (Kubiak et al. 2014; Sokół et al. 2015a), and its signal is only slightly modified by the magnetospheric foreground if data selection is carried out

carefully (Galli et al. 2014, 2015). In the present analysis, we used observations from this portion of the Earth's orbit. To maintain as much year-to-year repeatability of the observation conditions as possible, we adopted a common criterion for the orbit selection: we chose those *IBEX* orbits with the spin axis pointing within the range of ecliptic longitudes (235°, 295°), i.e., from mid-November of the year preceding the given season year to the end of January. This choice effectively included all of the orbits where the WB signal is clearly visible, and by design it ends at the beginning of the range chosen by Bzowski et al. (2015) for the analysis of the primary ISN He. The data used were collected during the *IBEX* ISN gas observation campaigns during 2010–2014 because the commissioning of the spacecraft during the 2009 *IBEX* ISN season was completed too late to observe the Breeze. We use the histogram-binned data product, corrected where needed for the instrument throughput reduction (Möbius et al. 2015b; Swaczyna et al. 2015), and take the Golden Triples events, i.e., we only take those events with three time-of-flight measurements that are almost certainly due to H^- ions. The data are binned into 60 equal-width bins covering the full 360° range of *IBEX* spin angles. A connection between the *IBEX* spin angles and the absolute directions in the sky for individual orbits is presented in Figure 2 in Sokół et al. (2015a; see also the transformation matrix given in Equation (22) in Sokół et al. 2015b, and the spin axis orientation in Swaczyna et al. 2015).

The selection of data from individual orbits was carried out using the same criteria as for the ISN He observations reported by Bzowski et al. (2015), Leonard et al. (2015), McComas et al. (2015a), Möbius et al. (2015b), Schwadron et al. (2015a), and Swaczyna et al. (2015). A summary of this coordinated analysis is given by McComas et al. (2015b). In brief, these criteria rejected the data intervals with synchronization issues, with known magnetospheric contamination, and with excessive signals observed in other *IBEX* energy channels. Details of good time selection were presented by Fuselier et al. (2014), Galli et al. (2014), and Galli et al. (2015), as well as Leonard et al. (2015) and Möbius et al. (2015b). The good time intervals used in our analysis are presented in Figure 1.

The final step in our data selection was choosing the spin angle range. The WB signal is visible in energy channels 1, 2, and 3, but the signals for individual energy channels differ from each other (Figure 2). These differences are most likely due to the different energy sensitivities of *IBEX*-Lo in different energy channels. On one hand, the absolute levels of the signal vary from one energy channel to another, while on the other hand, the fall off in the wings of the signal seems to start at the spin angles that depend on the energy of the incoming atom. In principle, such differences are expected, as shown by modeling by Kubiak et al. (2014) and Sokół et al. (2015a) and observed in the measurements by Galli et al. (2015). The signal falls off for those spin angles where atoms with lower energies enter the instrument, but for each orbit there is an interval of spin angles where the flux does not depend on the adopted energy threshold regardless of the magnitude of the latter within all of the reasonably expected values.

A potentially important difference between our simulations and the actual measurement process is that while the simulation calculates the flux of neutral He atoms hitting the instrument and its collimation by the *IBEX*-Lo collimator (Sokół et al. 2015b), it does does not emulate any processes related to the conversion of the He atom flux into the count rate of the H^- ions that *IBEX*-Lo registers other than a sharp cutoff at the lower end of the energy spectrum of the incoming atoms. The He atoms hitting the instrument predominantly have kinetic energies much larger than the boundaries of the three lowest energy channels of *IBEX*-Lo, and the sputtered H^- ions are expected to have a roughly flat energy spectrum in the energy range corresponding to the energy ranges of at least *IBEX* energy channels 1 and 2 (see Figure 1 in Möbius et al. 2012 and Saul et al. 2012). Therefore, it is expected that even though the absolute magnitudes of the count rates measured in channels 1 and 2 may systematically differ, the shapes of the signal as a function of spin angle should be very similar. Departures may suggest that some of the signal is not due to sputtering by He atoms (e.g., a local foreground) or that the spectrum of the sputtering products is not flat, e.g., because of a finite energy threshold for the sputtering. Therefore, we chose the spin angle range where the count rates in energy channels 1 and 2 tracked each other well (i.e., we rejected the parts where the signal started to precipitously fall off, as expected for a finite energy threshold; see Figures 8 and 9 in Kubiak et al. 2014, and Figure 10 in Sokół et al. 2015a). Another consideration was finding a common spin angle range for all of the orbits included in this study. This was important because, on one hand, we suspect that the data may still contain some remnant foreground and, on the other hand, the width of the signal in the spin angle space narrows toward later orbits. Maintaining identical numbers of data points for all of the orbits guarantees that no orbit is statistically biasing the results because of the number dominance of data points it contributes to the global sample. These considerations resulted in the adoption of data from energy channel 2 from the spin angle range from 216° to 318°, i.e., 18 data points per orbit. The data selected are shown in the upper panes of the panels in Figure 4.

In principle, we could have chosen energy channel 1 instead of 2. However, as shown by Saul et al. (2012), energy channel 1 in the ISN orbit range contains an appreciable contribution from ISN H, with channel 2 affected much less (see also Schwadron et al. 2013; Katushkina et al. 2015). This component is not expected in the orbits from the WB range (however, see the Discussion later in the text), but to infer the abundance of the WB we must use the scaling factors between the simulated flux and the measured count rate, obtained for ISN He for each observation season. These factors were found in the fitting of the ISN He parameters by Bzowski et al. (2015), who used data from energy channel 2.

To test the robustness of our results, we also used data from extended and narrowed spin angle ranges, 204°–330° and 228°–306°, respectively, and, additionally, the spin angle range covering the entire ram hemisphere: 180°–354°. In the two extended ranges, we do expect some dependence of the signal on the sputtering threshold, and therefore throughout the simulations we adopted a value for this threshold equal to 38 eV, which is consistent with the results of the analysis by Galli et al. (2015).

3. ANALYSIS

In this section we present our analysis. We start by presenting the physical model for the WB phenomenon we adopted, the preparation of the data selected in the previous section for parameter fitting, and the aspects of the measurement process that affect the data measurement uncertainty and

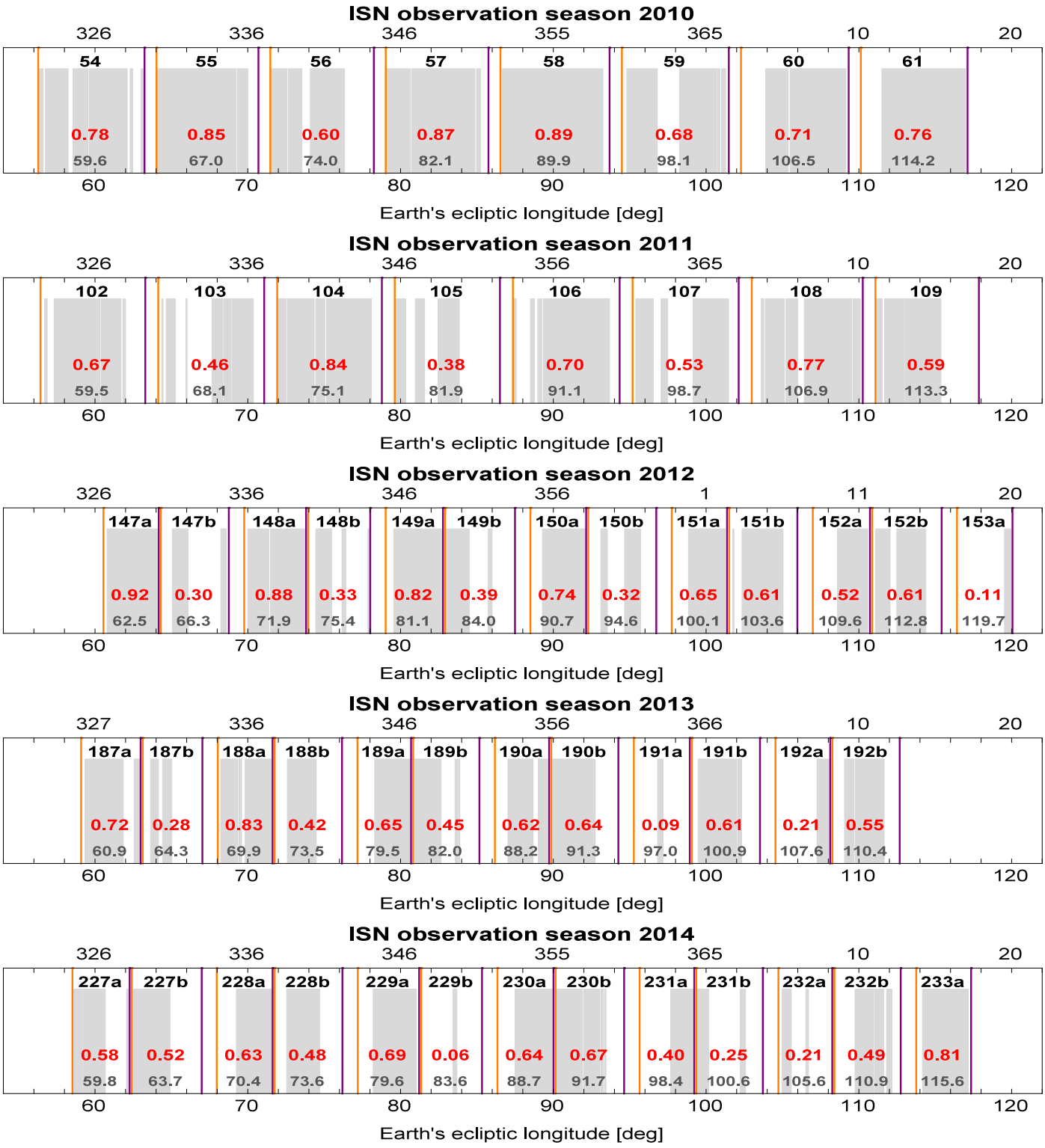

Figure 1. Distribution of good time intervals during the *IBEX*-Lo observations of the Warm Breeze adopted for the analysis. The format of the figure is similar to that of Figure 1 in Bzowski et al. (2015). The gray regions mark the individual good time intervals. The orange bars mark the beginning and the purple bars the end of the High-Altitude Science Operations (HASO) intervals when the *IBEX* measurements were actually carried out. The thick black labels mark individual orbits (or orbital arcs, in the 2012–2014 seasons). The red numbers (in the middle row) mark the fraction of HASO intervals occupied by the good time intervals for a given orbit. In the lower row, the approximate longitudes of the spacecraft during a given orbit are marked (actually, it is the Earth longitude averaged over the ISN good time for an orbit). They can be used to identify an approximate correspondence between orbits from different seasons. The lower horizontal axes are scaled in the Earth's ecliptic longitude and the upper horizontal axes are scaled in days of the calendar year (note that a new year begins during each individual Warm Breeze observation season).

correlations between individual data points. Then, we discuss the method of fitting parameters and assessing their uncertainties; the correlations between the parameters are also presented. We also discuss the residuals and their implications. Finally, we present additional tests of the robustness of the results and derive the uncertainties and correlations of the WB parameters.

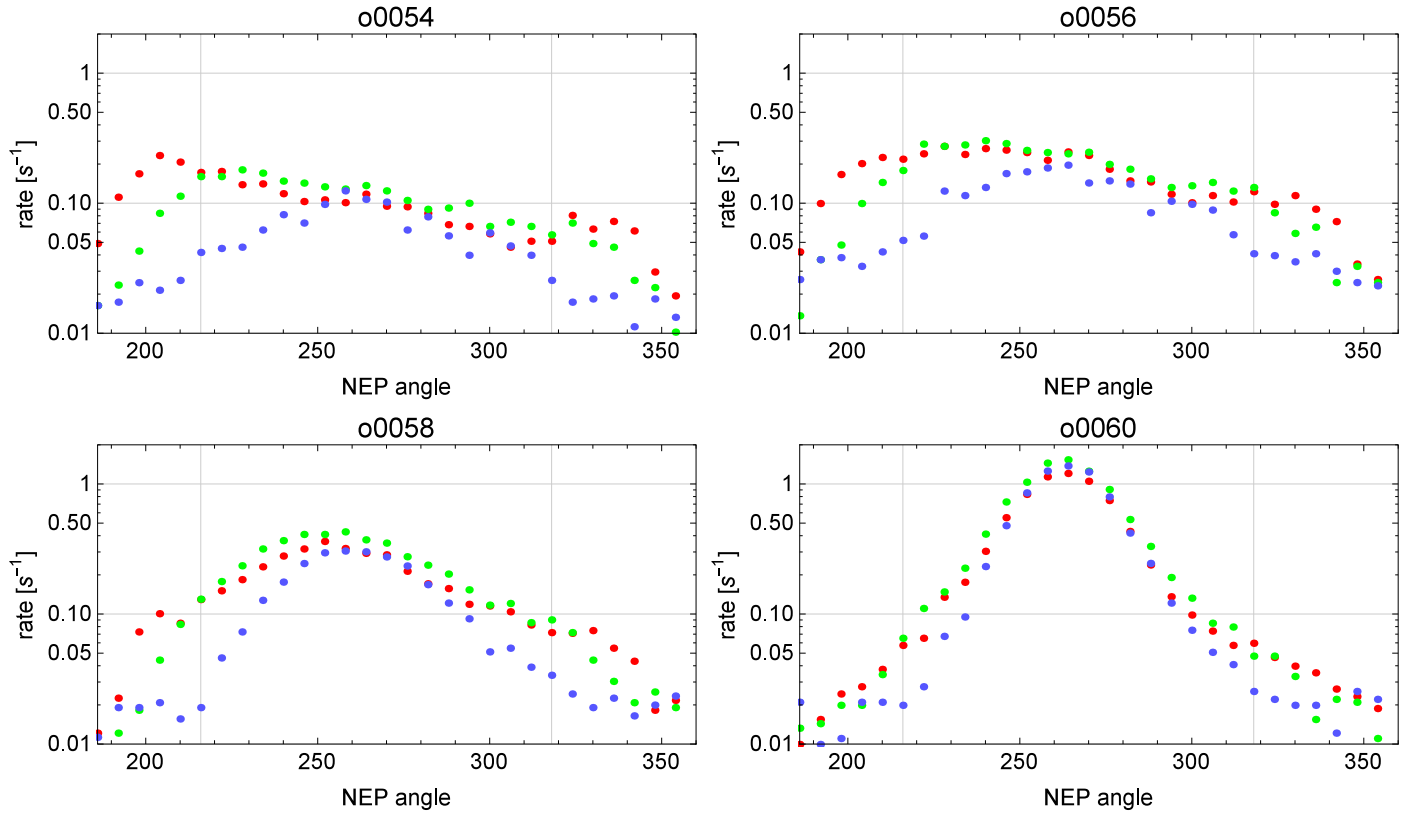

Figure 2. Count rates observed in four orbits from the Warm Breeze observation season 2010 as a function of spin angle. Unlike in Figure 4, no background and ISN He subtraction have been performed. Each dot represents the good-time averaged count rate for an individual 6° pixel. The colors symbolize different *IBEX*-Lo energy steps: red—channel 1, green—channel 2 (used in the fitting), and blue—channel 3. The vertical bars mark the interval of spin angles selected for the baseline fitting. The interval shown is from spin angle 180° to 354°, i.e., the wider interval used in the complementary fit (see the text). The four orbits are chosen out of the eight orbits from this observation season used in the analysis as illustrative examples. Note that the count rate variations with the spin angle for energy channels 1 and 2 are similar to each other, while energy channel 3 features clear deviations from the other two channels. The behavior of the data from the other observation seasons is similar.

3.1. The Physical Model, Uncertainty System, and Data Preparation

We carried out our analysis using the method, data uncertainties, and data correlation system presented in detail by Swaczyna et al. (2015) These aspects of the analysis are similar to those in the determination of the inflow parameters of the primary ISN He population by Bzowski et al. (2015). All of the data used had been corrected for the throughput reduction in the instrument interface, following the scheme presented in detail by Swaczyna et al. (2015), except for the data from the 2013 and 2014 seasons, for which the correction is not needed due to an on board software change. The magnitudes of the correction and their uncertainties were calculated based on the actually measured data.[6]

The uncertainty system used in the calculation of the data covariance matrix includes the statistical uncertainty of the Poisson counting process (uncorrelated between the data points), the background (assumed to be constant for all data points and thus correlating them), the uncertainty of the spin axis (which correlates points from individual orbits), the uncertainty of the *IBEX*-Lo boresight orientation with respect to the spin axis (identical for all orbits, it correlates all data points), and the uncertainty of the throughput correction. The closing element of the uncertainty system is the uncertainty of the primary ISN He model, which was adopted as obtained from the analysis of ISN He by Bzowski et al. (2015). Before fitting, we subtracted the simulated signal from the ISN He primary population from the data. We also subtracted the constant level of the ubiquitous background, adopted after Galli et al. (2014) at $(8.9 \pm 1.0) \cdot 10^{-3}$ cts s^{-1} for observation seasons 2010–2012 and to $(4.2 \pm 0.5) \cdot 10^{-3}$ for the 2013 and 2014 seasons, i.e., after the PAC voltage reduction (Möbius et al. 2015a), identically to what was done by Bzowski et al. (2015). The ISN He signal was calculated precisely for the actual observation conditions and using the yearly scaling factors that were fitted by Bzowski et al. (2015) together with the ISN He inflow parameters. This was needed to exactly reproduce the observed count rates.

The ISN He signal subtracted from the data and the signal from the WB were simulated using the latest version of the Warsaw Test Particle Model, presented in detail by Sokół et al. (2015b) with the time-dependent photoionization rate from Sokół & Bzowski (2014). The physical model of the neutral He gas observed by *IBEX* is a superposition of a neutral He flux at Earth's orbit originating from two Maxwell–Boltzmann populations of neutral He atoms in front of the heliosphere: the primary ISN He population, with the temperature and inflow velocity vector in the source region as reported by Bzowski et al. (2015) for the fit to the ISN He data from all seasons ($\lambda_{\rm ISN} = 255\overset{\circ}{.}75$, $\beta_{\rm ISN} = 5\overset{\circ}{.}16$, $v_{\rm ISN} = 25.76$ km s^{-1},

[6] For some ISN orbits in the 2011 and 2012 seasons, the precise value of the correction could not be calculated due to a special observation mode of the instrument, as explained by Möbius et al. (2015a), and an average value was used instead, but for the data used here in the WB parameter fitting, no such approximate measures were needed.

Table 1
Fit Results Depending on Spin Angle Selection

Case	$\lambda(^\circ)$	$\beta(^\circ)$	v (km s^{-1})	T (K)[a]	M	ξ	N_{dof}[b]	χ^2_{min}	χ^2_{min}/N_{dof}
228°–306°	251.96 ± 0.65	12.64 ± 0.34	11.44 ± 0.57	10,450 ± 1190	1.90 ± 0.04	0.062 ± 0.004	747	1443.92	1.933
216°–318°[c]	251.57 ± 0.50	11.95 ± 0.30	11.28 ± 0.48	9480 ± 920	1.97 ± 0.04	0.057 ± 0.004	963	1821.80	1.892
204°–330°	250.22 ± 0.45	11.47 ± 0.30	12.38 ± 0.48	11,620 ± 1000	1.95 ± 0.03	0.065 ± 0.004	1179	2341.95	1.986
180°–354°	249.39 ± 0.44	11.40 ± 0.29	11.98 ± 0.45	11,100 ± 980	1.93 ± 0.03	0.064 ± 0.004	1611	3312.51	2.056

Notes. The uncertainties obtained from the fits have been scaled up by a factor of $\sqrt{\chi^2_{min}/N_{dof}}$ to acknowledge the values of minimum χ^2 significantly exceeding the statistically expected values. The uncertainty of the expected value of minimum χ^2 is equal to $\sqrt{2N_{dof}}$.
[a] Rounded to 10 K.
[b] Number of degrees of freedom in the fit.
[c] The baseline spin angle range selection (see text).

$T_{ISN} = 7440$ K), and another Maxwell–Boltzmann population, corresponding to the WB, with the parameters being sought. These latter parameters include a temperature T_{WB}, a velocity vector (v_{WB}, λ_{WB}, β_{WB}), and an abundance ξ_{WB} relative to the primary ISN He population. In the actual fitting, the temperature was replaced with the mean square of the thermal velocity, defined as $v_{T,WB} = \sqrt{3k_B T_{WB}/m_{He}}$. The parameters of both populations were assumed to be homogeneous in the source region in front of the heliosphere, and the distance to the source (i.e., the distance of tracking the test atoms in the model) was set to 150 au from the Sun. Discussion of the reasons for this choice of the source distance and of its very small influence on the results for the ISN He gas can be found in McComas et al. (2015b) and Sokół et al. (2015b). The relatively small tracking distance for the WB population, which places the source region just beyond the heliopause, is especially reasonable for the hypothesis that the WB is the secondary component of ISN gas that would be formed at roughly such a distance, but the parameter values we have obtained are not very sensitive to this choice. We assumed that the velocity vector and temperature of the WB in the source region do not change with time, but—because some measurement aspects varied between the observation seasons, as explained in detail by Bzowski et al. (2015)—we allowed the abundance parameter to vary from year to year, i.e., we adopted five free abundance parameters, used for the five yearly data subsets. Hence, the total number of fit parameters was equal to nine. The abundance parameters were fitted analytically, as described by Sokół et al. (2015b), and were not part of the parameter grid discussed below.

3.2. Parameter Fitting

The WB parameter fitting was carried out in a two-step process. In the first step, we used a simplified fitting to approximately determine the parameter correlation line for the solution. This was done using a method similar to that employed by Kubiak et al. (2014) in the WB discovery paper. In this method, a simplified uncertainty system was used, including only the statistical uncertainty of the signal and the uncertainty of the background. The fits were carried out for the data with the background and the model of the ISN He population subtracted. They were performed for two spin angle ranges: 222°–312° and 186°–354°.

Subsequently, with the approximate parameter correlation lines established and an approximate best-fit solution found, we defined a regular grid of parameters in the four-dimensional (4D) parameter space to carry out the calculations needed to obtain the data correlation matrix as described by Swaczyna et al. (2015). Based on the simplified fitting, we selected the range of ecliptic longitudes between 237° and 259° with a step of $\Delta\lambda = 2^\circ$. For the remaining parameters, we decided to adopt the following steps of the grid: $\Delta\beta = 0.^\circ5$, $\Delta v_T = 0.5$ km s^{-1}, and $\Delta v = 0.5$ km s^{-1}. For each ecliptic longitude of the original grid, we selected a point (β_0, v_{T0}, v_0) that was nearest to the minimum χ^2 for this longitude and had coordinates that were integer multiples of the planned step of the grid. The grid nodes were constructed so that for each longitude, we found points $(\beta_0 + n_\beta \Delta\beta, v_{T0} + n_{v_T} \Delta v_T, v_0 + n_v \Delta n_v)$ such that for integer values of n_β, n_{v_T}, and n_v the condition $\sqrt{n_\beta^2 + n_{v_T}^2 + n_v^2} < 4.5$ was fulfilled. Thus, we end up with a total of 4668 grid nodes around the expected correlation line.

With the parameter grid defined, we carried out simulations of the WB flux observed by *IBEX* using the parameters from the grid nodes. The simulations were carried out for the entire range of spin angles from the upwind hemisphere, so that we were able to select the spin angle range for the parameter fitting relatively easily. Then, for a selected spin angle range, we compared the simulations with the data using the data covariance matrix and found the best-fit parameters with their covariance matrix as proposed by Swaczyna et al. (2015). Based on this, we calculated the parameter uncertainties and correlations. In addition to the baseline fit, we performed additional test fits for the full ram hemisphere and for two additional spin angle ranges: one narrower by four data points per orbit, and another one for a spin angle range wider by four data points. This was done to test the robustness of the results. The results of the fitting are listed in Table 1.

3.3. Results and Discussion

Fitting the parameters provided the best-fit solution $\lambda_{WB} = 251.^\circ573$, $\beta_{WB} = 11.^\circ954$, $v_{WB} = 11.284$ km s^{-1}, $v_{T,WB} = 7.659$ km s^{-1}. The temperature is thus $T_{WB} = 9475$ K and the Mach number of the flow is $M_{WB} = 1.97$. The abundances obtained for individual seasons were $(5.72 \pm 0.29, 6.00 \pm 0.30, 5.79 \pm 0.29, 5.63 \pm 0.30, 5.21 \pm 0.28) \cdot 10^{-2}$. The resulting abundance, calculated as a weighted arithmetic mean value of the abundances obtained for individual seasons, is $\xi WB = 5.66 \cdot 10^{-2}$. The parameters form a "tube" in parameter space, similar to what was found in the case of *IBEX* observations of the ISN He population. The covariance matrix

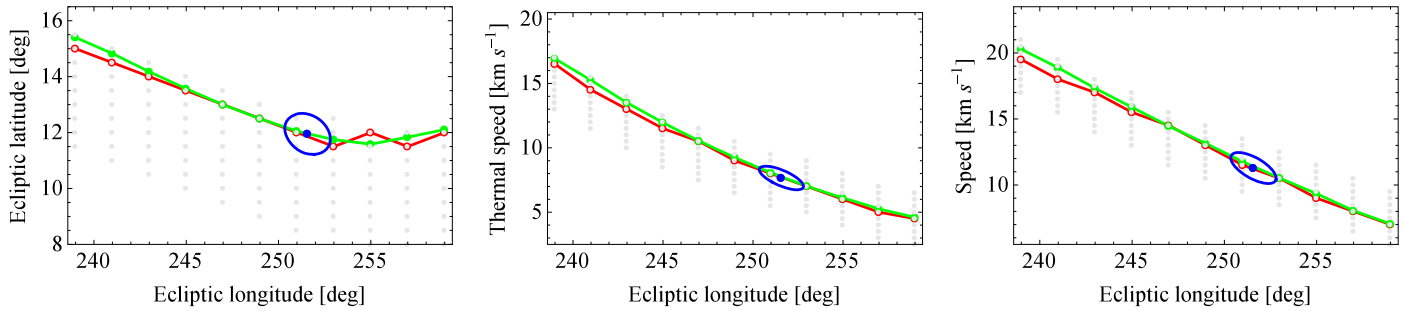

Figure 3. Parameter correlation lines projected into 2D subspaces of the 4D parameter space, as a function ecliptic longitude. The gray dots are the simulation grid points. The red line connects the grid points for which the minimum χ^2 value was obtained for a given longitude. The green line connects the results of inter-grid optimization, i.e., the χ^2 minima found for the parameter subspaces deployed around the given node in longitude. The blue dots represent the locus of the absolute minimum of χ^2 listed in the second row of Table 1 and the blue ellipses are the contours of projections of the 2σ 4D ellipsoid on the 2D parameter subspaces.

of the solution is the following:

$$\mathrm{Cov} = \left(\begin{array}{c|cccc} & \lambda\ [^\circ] & \beta\ [^\circ] & v_\mathrm{T}\ [\mathrm{km\ s^{-1}}] & v\ [\mathrm{km\ s^{-1}}] \\ \hline \lambda & 0.1301 & -0.01922 & -0.06892 & -0.08179 \\ \beta & -0.01922 & 0.04622 & 0.01114 & 0.001917 \\ v_\mathrm{T} & -0.06892 & 0.01114 & 0.07282 & 0.08692 \\ v & -0.08179 & 0.001917 & 0.08692 & 0.1187 \end{array}\right). \quad (1)$$

This matrix includes the formal uncertainties resulting from the fitting. These uncertainties are very small, e.g., the uncertainty of the inflow direction is equal to $\sqrt{0.1301}^\circ = 0.^\circ36$ and the uncertainty of the inflow latitude is $\sim 0.^\circ22$. The correlations between the parameters are described by the following correlation matrix:

$$\mathrm{Cor} = \begin{pmatrix} 1 & -0.2479 & -0.7082 & -0.6584 \\ -0.2479 & 1 & 0.1920 & 0.02588 \\ -0.7082 & 0.1920 & 1 & 0.9350 \\ -0.6584 & 0.02588 & 0.9350 & 1 \end{pmatrix} \quad (2)$$

and illustrated in Figure 3. The strongest correlation, 0.935, exists between the inflow speed and thermal velocity. The weakest correlation is for the parameter pairs including the inflow latitude (see the second row in the correlation matrix). The inflow longitude is relatively strongly anticorrelated with the thermal velocity, and also with the inflow speed due to the strong correlation of the latter with the inflow speed. A similar pattern of correlations was observed by Bzowski et al. (2015) for ISN He. Projections of the 4D correlation line and of the grid points on 2D subspaces are presented in Figure 3. The content and format of this figure are very similar to those of Figure 5 for the primary ISN He flow in Bzowski et al. (2015).

The minimum χ^2 value obtained from the fitting is equal to $\chi^2_\mathrm{min} = 1821.80$ for the number of degrees of freedom $N_\mathrm{dof} = 963$, which suggests that the fit quality is unsatisfactory because the minimum χ^2 obtained is much greater than the statistically expected value, which is equal to $N_\mathrm{dof} \pm \sqrt{2N_\mathrm{dof}} = 963 \pm 43.9$. As discussed by Swaczyna et al. (2015), a situation where the minimum χ^2 significantly exceeds the statistically expected value is not unusual in physics and astrophysics. The possible reasons include underestimated data uncertainties, inadequate/incomplete interpretation model, or an additional signal in the data not accounted for in the analysis. Such a situation was also encountered by Bzowski et al. (2015), who decided to adopt a procedure of scaling up the uncertainties by multiplying them by the square root of reduced χ^2, i.e., by $\sqrt{\chi^2_\mathrm{min}/N_\mathrm{dof}}$. This uncertainty scaling was suggested, among others, by Olive et al. (2014). In our case, $\chi^2_\mathrm{min}/N_\mathrm{dof} \simeq 1.9$, and so the uncertainties should be multiplied by a factor of $\sim$1.4. We perform this scaling again here and list the results as the parameter uncertainties in Table 1, but we refrain from adopting these uncertainties as the final for our parameters because of the reasons explained later in this section.

As for the primary ISN population (Bzowski et al. 2012, 2015; McComas et al. 2012), the correlation between the parameters results in a very elongated, deep minimum of χ^2 in parameter space. The blue lines in Figure 3 illustrate the isocontours for the χ^2 value equal to $\chi^2_\mathrm{min} + 6.2 \cdot 1.9$, corresponding to the region of 2σ uncertainty, scaled by the minimum reduced χ^2 value to acknowledge the uncertainty scaling descibed previously. All of the χ^2 values outside the regions marked by the blue contours in Figure 3 are larger.

The direct cause of the high value of the minimum χ^2 can be inferred from inspection of Figure 4. While the best-fit model generally reproduces the observed signal quite well, two intervals of ecliptic longitudes can be identified where the best-fit solution systematically deviates from the data. The most conspicuous of them begins at $\lambda \simeq 95^\circ$ (orbit 59 and the equivalent ones from the subsequent seasons, see also Figure 1). Approximately six data points near the center of the spin angle range in those orbits show an excess of the data over the model, which systematically increases with the increasing Earth longitude, even though the normalized residuals do not look that bad in this region because of the large uncertainties of the data there. The remaining data points from these orbits do not show any systematic deviations. While the statistics in this interval are best during an individual observation season (relatively large count numbers registered), the uncertainty is large because the signal in this region has a large contribution from the primary ISN He population, which is practically absent in the data collected in the earlier portion of the Earth's orbit. An application of the uncertainty system from Swaczyna et al. (2015) results in the relatively large uncertainties in the count rate left for fitting the WB after subtraction of the primary ISN He model.

Another region where the residuals are relatively large is the Earth longitude range below $\sim 75^\circ$ (orbits 56 and earlier, as well as their equivalents in the following seasons). In this region, the residuals are also predominantly positive, especially in the

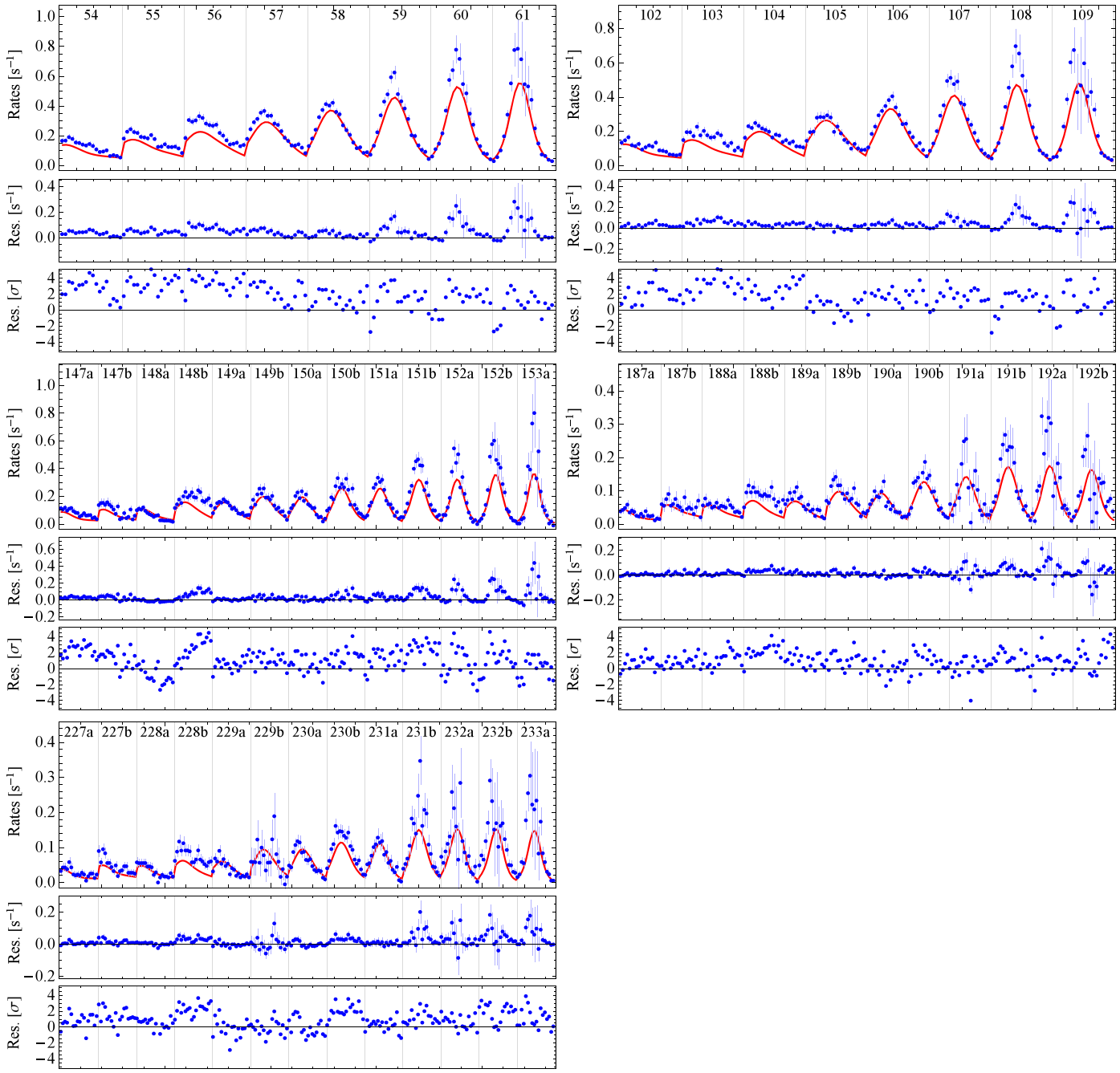

Figure 4. Comparison of the data (upper panes, blue dots with error bars) with the best-fit model (red line), and the residuals: absolute (middle pane) and normalized (i.e., the absolute residuals divided by the total uncertainty; lower panes) for all five observation seasons analyzed, from 2010 (upper left) to 2014 (lower left). The vertical bars partition the panels into fragments corresponding to individual orbits, whose numbers are listed at the top of the upper pane of each panel. The horizontal axis is the data point number in the analyzed sample for this observation season. The spin angle range, identical for all of the seasons, is from 216° to 318° and one data point corresponds to a 6° accumulation bin.

2010–2012 seasons, but the statistics of the observed atoms are the lowest in the sample. This excess of the signal over the model can be understood based on analysis by Galli et al. (2014), who suggested that remnants of the magnetospheric foreground may persist in this region, despite all of the filtering procedures applied. An argument in favor of this hypothesis may be a reduction of this phenomenon in the data from 2013 and 2014, i.e., after the reduction of the post-acceleration voltage (Möbius et al. 2015b).[7] The magnetospheric contamination is believed to be mostly due to H atoms (the dominant ENAs emitted by the magnetosphere), and their energy seems to mostly be in energy channels 1 and 2. The helium atoms from the WB are more energetic. The reduction in the PAC voltage resulted in a decrease in the sensitivity of *IBEX*-Lo, and the reduction seems to be stronger for the atoms with lower energies. Hence, a likely hypothesis to explain the behavior of the residuals is the disappearance of the magnetospheric

[7] Note that the vertical scales in the upper and middle panes of the yearly panels in Figure 4 are adjusted to follow the actual amplitude of the signal, which is reduced in 2013 and 2014.

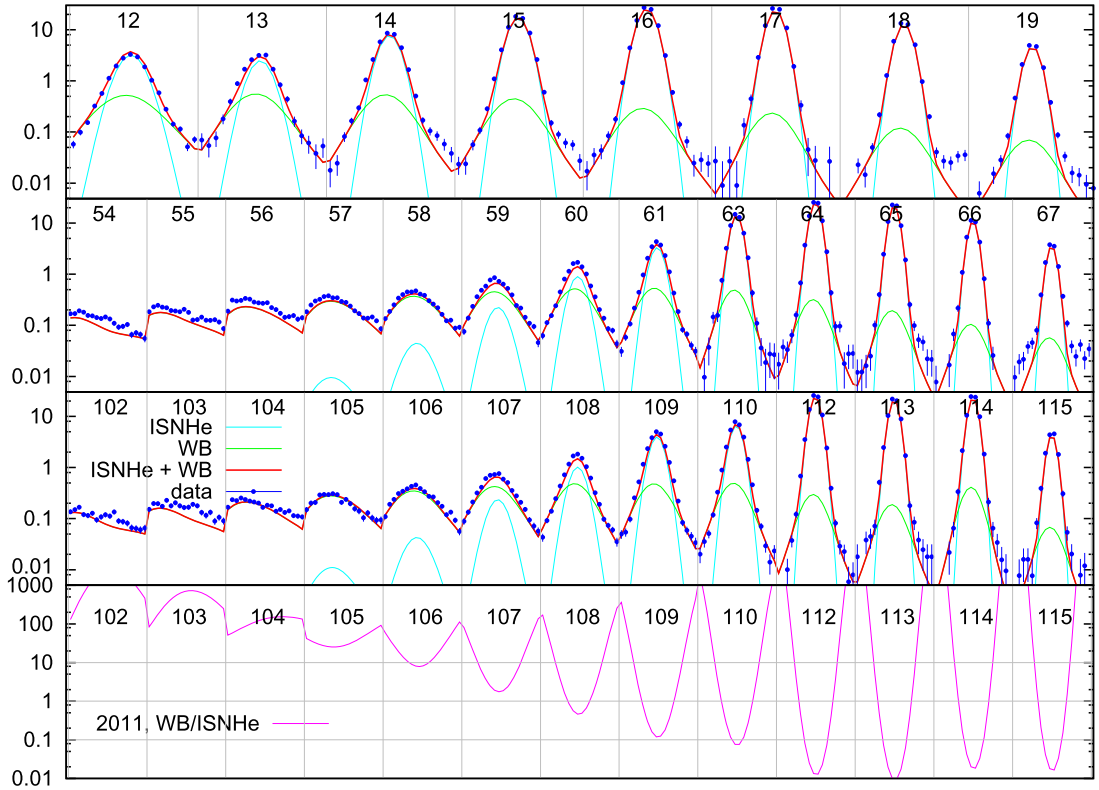

Figure 5. Comparison of the data and the full model including the primary ISN He and the Warm Breeze, for the orbits from the 2009–2011 ISN observation seasons used by Bzowski et al. (2015) for the analysis of ISN He (orbit # ⩾14 for 2009, ⩾63 for 2010, and ⩾110 for 2011), as well as the available earlier orbits, for the spin angle range 216°–318°. Note that none of the data points from the 2009 season were used for fitting the Warm Breeze parameters. The spin angle range used by Bzowski et al. (2015) for the ISN He analysis is 252°–282°, which corresponds to the center six points for orbits 14 through 19 and their equivalents from the later seasons. The data points are arranged in the increasing order of their respective spin angles, the subsets corresponding to individual orbits are partitioned by the vertical bars. The vertical axis is scaled in counts per second. The cyan line represents the model of the primary ISN He, the green line represents the model of the Warm Breeze, and the red line corresponds to the sum of the latter two components. The blue symbols represent the measured count rates (with the constant background subtracted) and their uncertainties. The lower panel presents the ratio of the flux due to the Warm Breeze to the flux due to ISN He for the 2011 season. For the other seasons, details of this ratio are different, but the general behavior does not change.

foreground in the data due to the instrument becoming less sensitive to this component.

Another hypothesis, which is complementary to the former one, is that the residual is due to ISN H. Saul et al. (2012) and Schwadron et al. (2013) pointed out that the core of the ISN H contribution to the signal observed in the lowest energy channels of *IBEX*-Lo is observed in orbit 23 and the corresponding ones during the solar minimum epoch, and that this signal fades during the epoch of high solar activity due to an increased level of repulsive solar radiation pressure. However, an analysis by Kubiak et al. (2013) suggests that a non-zero flux from ISN H (calculated as a superposition of the primary and secondary populations) is expected throughout the entire ISN observation season (see their Figure 3) and that the maximum intensity of this signal for orbits 55 through 58 should be only a little lower than that of the primary ISN He. The ISN H flux for these orbits is expected to be at a level of a few times 10^{-4} of the signal expected for ISN He at the seasonal peak intensity, i.e., at a level comparable to the level of the signal from ISN He. The latter one for these orbits, as seen in the lower panel of Figure 5, is at a level of 0.01 of the WB signal. This makes the hypothetical contribution from ISN H to the residuals of our present model of the WB of a similar order of magnitude to what we actually observe. Furthermore, Kubiak et al. (2013) predict an appreciable reduction of the ISN H flux during the times of high solar activity, and the residuals that we obtained for the seasons of high solar activity are indeed lower for this portion of the Earth's orbit. This topic certainly deserves further study because, on one hand, the calculations by Kubiak et al. (2013) were carried out with assumptions similar to those made by Katushkina et al. (2015), and on the other hand, Katushkina et al. (2015) showed, using a very sophisticated model of ISN H, that these assumptions lead to a simulated signal very different from the signal actually observed for the orbit where the ISN H flux maximum is expected. To narrow this gap, these authors had to significantly modify the radiation pressure used in the simulations. The consequences of this modification for the ISN H flux expected on the orbits we discuss now, i.e., 54–57 and the equivalent from the other seasons are unknown. However, further investigation of this aspect is beyond the scope of our paper.

Following the same argument, the excess of the data above the simulation at the large longitude at the end of the data set is likely due to the primary ISN He atoms. In this case, despite the reduction of the PAC voltage and the increased level of solar activity, the excess has not disappeared, and so this excess is very likely due to He atoms, not H atoms. A non-perfect reproduction of the ISN He population in our analysis can, in fact, be expected based on the insight provided by Bzowski et al. (2015). They pointed out that the parameters of the ISN He model they obtained may have been biased due to an imprecise knowledge of the WB parameters. These parameters

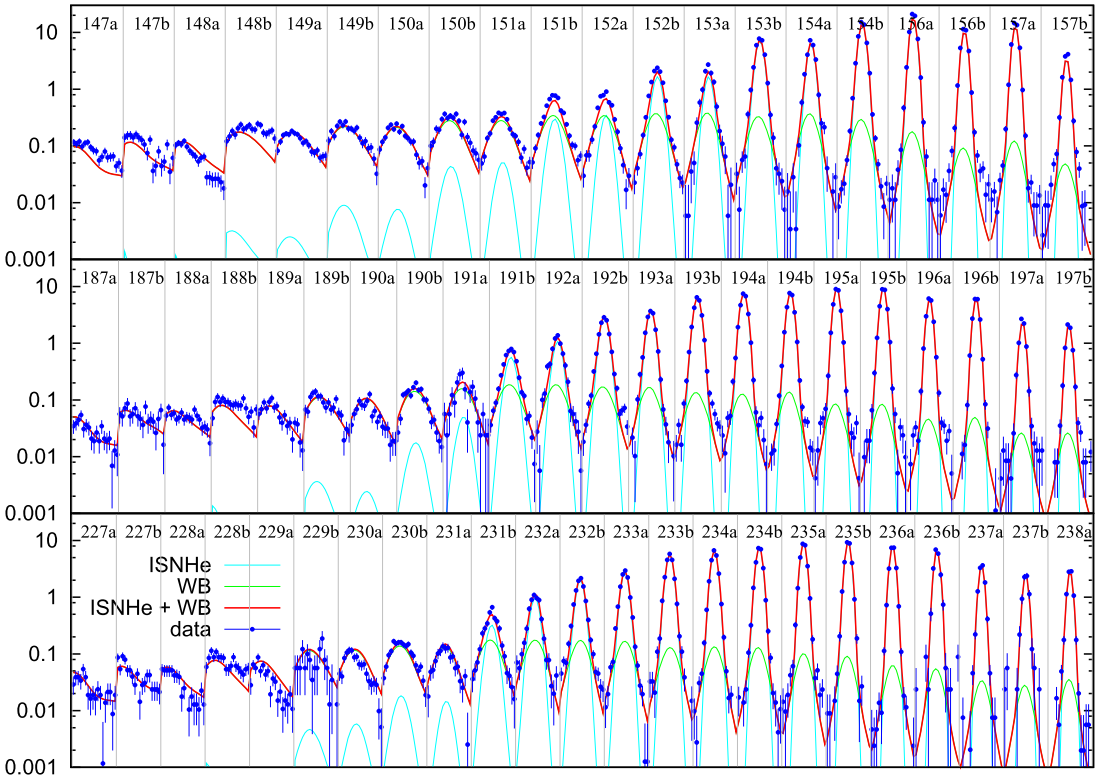

Figure 6. Comparison of the data and the full model including the primary ISN He and the Warm Breeze, for the orbits from the 2012–2014 ISN observation seasons used by Bzowski et al. (2015) to fit the ISN He parameters (orbit # ⩾153b, ⩾193a, and ⩾233b for the three seasons, respectively) and for the orbits used now in the Warm Breeze fitting, for the spin angle range 216°–318°. The color and symbol code are identical to that in Figure 5. Note the consistently lower levels of the signal in 2013 and 2014 because of the reduction in the PAC voltage introduced after the 2012 ISN season.

were imprecise, as was suggested by these authors, and as can be seen from our present analysis. On the other hand, statistically speaking, the only evidence for this excess is the visible correlation between the positive absolute residuals for Earth longitudes larger than ∼90°, since the magnitude of the normalized residuals is not significantly larger than in the remaining portion of the data.

The agreement between the data and the model of the neutral He signal is good even for the orbits that were not used in the WB fitting. This is illustrated in Figures 5 and 6. Even though the ISN He model was only fit to the six center points for each of the orbits used by Bzowski et al. (2015), and the WB fitting did not use the data from these orbits at all, the agreement between the data and the sum of the ISN He and WB populations is evident and most of the small deviations seem to be random. They typically occur at the boundaries of the spin angle range where a contribution from the local foreground may still be present. Inspection of the lower panel of Figure 5, which shows the ratio of the WB flux to the ISN He flux, reveals the balance between the two populations in different orbits and different spin angles, and confirms the choice of data by Möbius et al. (2015a), Leonard et al. (2015), Swaczyna et al. (2015), Schwadron et al. (2015a), and Bzowski et al. (2015) for their analyses of the primary ISN He flow: the data they used contain relatively little contribution from the WB. Simultaneously, it can be seen that a small remnant contribution was still present, as suspected by Bzowski et al. (2015) and Möbius et al. (2015a).

A more fundamental reason for the high value of the χ^2 minimum may be a weakness of the adopted model for the parent population. We approximate this population with a Maxwell–Boltzmann distribution function with spatially homogenous parameters. However, if the WB is the secondary population of ISN He, created in the outer heliosheath, then this approximation is certainly not perfect and we expect significant spatial gradients in the flow speed, direction, and temperature of the parent gas. Therefore the parameters we derive in our analysis must be regarded as kinds of mean values, spatially averaged over the source region of the WB population. We speculate that such spatial gradients of the parent plasma parameters could be responsible for some systematic departures of the simulated signal from the data, and thus for the high value of the minimum χ^2 found.

To check the robustness of the solution, we reviewed the fit results for the additional spin angle ranges mentioned earlier (see Table 1). The two wider ranges included the portions of the data where the signal is expected to depend on the non-zero energy threshold of the sensitivity of *IBEX*-Lo, reported by Galli et al. (2015) to be at least ∼20 eV. It is evident that the fit parameters react to the change in the spin angle range adopted for the analysis. The absolute magnitude of the changes is larger than the uncertainties of the fitting, even after scaling them up. This is not surprising, since broadening the range of spin angles includes some data points affected by the uncertain sensitivity of the instrument to low-energy atoms. Relatively, the largest changes are seen in the temperature. Not surprisingly, the reduced χ^2 minimum, which is a measure of departure of the model from the data per degree of freedom, is larger when we include these additional data and is the lowest for the case we have selected as the baseline, which supports our choice.

We conclude from this test that the formal uncertainty estimates are too optimistic even after scaling them up to accommodate the high minimum χ^2 value. Therefore, in addition to the uncertainties resulting from the scaled-up covariance matrix, we also include uncertainties related to the poorly known drop in sensitivity for low energies. These additional uncertainties are estimated as the mean absolute values of the differences between the result of the baseline case and the cases listed in the first and third row in Table 1: $\Delta\lambda_{\rm WB} = 0.^\circ9$, $\Delta\beta_{\rm WB} = 0.^\circ6$, $\Delta v_{\rm WB} = 0.6\,{\rm km\,s^{-1}}$, $\Delta T_{\rm WB} = 1600$ K, $\Delta M_{\rm WB} = 0.05$, and $\Delta\xi_{\rm WB} = 0.007$.

Narrowing the uncertainty of the WB parameters will be possible once we better understand the sensitivity of the *IBEX*-Lo detector to He atoms with low energies. This requires carrying out a post-calibration on the spare version of the instrument, which is planned in the near future. With this additional calibration, we will hopefully be able to extend the data range into the spin angle regions affected by the decreasing instrument sensitivity for lower-energy atoms and to use data from two or hopefully three energy channels, which will further improve the statistics. For now, we adopt the uncertainty of the WB inflow parameters listed in row 2 in Table 1, additionally broadened by $\Delta\lambda_{\rm WB}$, $\Delta\beta_{\rm WB}$, $\Delta v_{\rm WB}$, $\Delta T_{\rm WB}$, $\Delta M_{\rm WB}$, and $\Delta\xi_{\rm WB}$, respectively: $\lambda_{\rm WB} = (251.57 \pm 0.50 \pm 0.9)^\circ$, $\beta_{\rm WB} = (11.95 \pm 0.30 \pm 0.6)^\circ$, $v_{\rm WB} = (11.28 \pm 0.48 \pm 0.7)$ km s^{-1}, $\xi_{\rm WB} = (5.7 \pm 0.4 \pm 0.7) \cdot 10^{-2}$. The temperature is $T_{\rm WB} = (9.48 \pm 0.92 \pm 1.6) \cdot 10^3$ K and the Mach number $M_{\rm WB} = 1.97 \pm 0.04 \pm 0.05$. The correlations between the uncertainties listed as the first ones are described by Equation (2).

The uncertainty range obtained in the present analysis of five *IBEX* WB observation seasons marginally overlaps with the uncertainty range provided by Kubiak et al. (2014) based on their analysis of the 2010 WB observation season alone. The most likely values obtained now differ in longitude by $\sim+11^\circ$ and in temperature by ~-5500 K, with the remaining parameters changed very little. The reasons for these differences are most likely (1) the improved data selection we adopted here compared to that by Kubiak et al. (2014), (2) the use by those authors of a much less precise version of the model of the ISN He population than is currently available (they used the ISN He parameters from Bzowski et al. 2012), and (3) the fact that the data set used in the present study was larger by a factor of five because now we have data from five observation seasons, not just one. Additionally, whereas Kubiak et al. (2014) used the data from the entire observation season, including the portion where the contribution from the primary ISN He population dominates, here we used solely the portion of the data not used by Bzowski et al. (2015) to fit the primary ISN He parameters.

4. IMPLICATIONS

Based on the insight gathered from this study, with all the uncertainties quantified, we can now propose a firm interpretation of the WB. This interpretation is based on two indirect pieces of evidence.

The first piece of evidence is the magnitude of the deflection of the WB inflow direction from the inflow of the primary ISN He inflow. Taking as the basis the ISN He direction obtained recently by Bzowski et al. (2015), who used a very similar fitting method to the method used here, we obtain the deflection of the WB from the primary ISN He equal to $7.^\circ9$. Such a deflection, as well as the temperature and inflow speed of the WB, are similar to the respective quantities predicted for the secondary ISN He by Kubiak et al. (2014; see their Figure 11) based on simulations that were carried out using the Moscow Monte Carlo model of the heliosphere (Izmodenov & Alexashov 2015) with interstellar parameters assumed very close to the parameters currently considered to be most accurate (Bzowski et al. 2015; McComas et al. 2015b; Schwadron et al. 2015a).

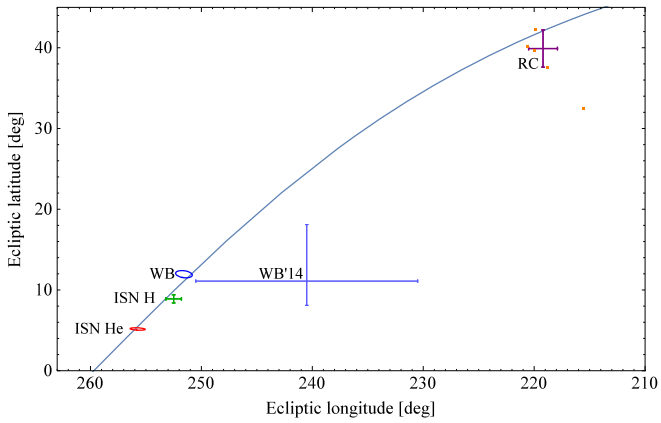

Figure 7. Comparison of selected important directions on the sky. WB is the inflow direction of the Warm Breeze from the best-fit model obtained in this paper, with the uncertainty ellipsoid. WB'14 is the Warm Breeze inflow direction obtained by Kubiak et al. (2014), with the error bars. ISN He denotes the best-fit solution for the ISN He inflow direction obtained by Bzowski et al. (2015) from the analysis of *IBEX* ISN He observations from 2009–2014. ISN H is the direction of inflow of ISN H with error bars, determined by Lallement et al. (2010) from analysis of SWAN/*SOHO* observations of the heliospheric backscatter glow; this direction corresponds to the average flow of the primary and secondary ISN H populations. The small orange squares are the directions toward the center of the *IBEX* Ribbon, determined by Funsten et al. (2013) from observations from *IBEX*-Hi energy channels 2 through 6 (note they form a monotonic sequence in ecliptic latitude, with the directions for *IBEX*-Hi energy channels 3 and 4, the closest to the solar wind energy, being the second and third from the top). The purple cross is the average direction for energy channels 2–4, with error bars. The blue line is the great circle fit to the directions of the Ribbon center, ISN He, ISN H, and the Warm Breeze (see Table 2).

The other piece of evidence is the observation that the *IBEX* Ribbon center (Funsten et al. 2013) and the directions of inflow that we have for the ISN He primary population (Bzowski et al. 2015), ISN H (i.e., a superposition of the primary and secondary populations, Lallement et al. 2005, 2010), and of the WB are now coplanar.

We fit a great circle on the sky to these four directions, using the uncertainty systems from Bzowski et al. (2015) and the present paper, the Ribbon center and its errors given by Funsten et al. (2013), ($\lambda_{\rm Ribbon} = 219.2^\circ$ $2^\circ \pm 1.^\circ3$, $\beta_{\rm Ribbon} = 39.^\circ9 \pm 2.^\circ3$), and the ISN H inflow direction and its uncertainty given by Lallement et al. (2010), ($\lambda_{\rm ISNH} = 252.5^\circ \pm 0.^\circ7$, $\beta_{\rm ISNH} = 8.^\circ9 \pm 0.^\circ5$). The fitted great circle is defined by its normal direction in the J2000 heliocentric ecliptic coordinates, equal to ($\lambda = 349^\circ \pm 0.^\circ6$, $\beta = 35.^\circ7 \pm 2.^\circ1$). This circle is plotted in Figure 7. The minimum χ^2 for this fit is equal to 3.59, while the statistically expected value is equal to 4.0 ± 2.8, which implies an excellent fit. As can be seen in Figure 7, the great circle goes through the uncertainty ranges of all four points used in the fit. It is evident from this figure that even if we adopted the WB inflow direction obtained from the fits to the wider ranges of

Table 2
Normal Directions to the H and He Deflection Plane and ***B*–*V*** Plane

Directions Used in Fit[a]	$\lambda(^\circ)$	$\beta(^\circ)$	ρ[b]
He, WB	348.85 ± 0.83	30.88 ± 3.89	0.92
He, H	350.16 ± 1.50	40.41 ± 8.02	0.97
He, WB, H	348.79 ± 0.84	31.35 ± 3.85	0.93
He, R	349.78 ± 0.60	37.88 ± 2.61	0.70
He, WB, R	349.80 ± 0.57	35.63 ± 2.06	0.82
He, WB, H, R	349.70 ± 0.56	35.72 ± 2.07	0.85

Notes.
[a] R—Ribbon, He—ISN He, H—ISN H, WB—Warm Breeze.
[b] Correlation coefficient obtained from fit.

spin angles instead of the one we have actually used, the resulting great circle would still go through the uncertainty ranges of all of the points used in the fits, and so the co-planarity conclusion would still hold.

The inflow directions of the ISN He and the WB form the so-called Helium Deflection Plane, with the normal vector listed in the first row of Table 2. This plane coincides within the uncertainties with the Hydrogen Deflection Plane, originally suggested by Lallement et al. (2005) and listed in the second row of Table 2 for the ISN He direction from Bzowski et al. (2015), very similar to the derivation by Witte (2004).

As discussed in the Introduction, this planar alignment of ISN He, ISN H, the WB, and of the center of the Ribbon can be naturally explained if the ISMF direction is the direction to the center of the Ribbon and—simultaneously—the WB is the secondary population of ISN He. Then, the WB direction is expected to be coplanar with a plane determined by the directions of the local ISMF and the ISN He inflow. To test the robustness of this hypothesis against evidence given by the available data, we calculated the normal directions to the plane fitted to the ISN He inflow directions from Bzowski et al. (2015) and various combinations of ISN H, Ribbon Center, and the WB direction obtained here. The results are collected in Table 2. They all agree with each other within their respective uncertainties, which supports the hypothesis that the WB is the secondary population of ISN He and that the Ribbon center coincides with the ISMF direction.

Adopting this hypothesis, we suggest that the so-called ***B*** **–** ***V*** plane, i.e., the plane including the ISMF vector and the flow vector of interstellar matter, is the plane obtained from fitting the directions of the Ribbon center and inflow directions of ISN He, ISN H, and the WB. The normal vector to this plane is given by the J2000 ecliptic coordinates $\lambda_{BV} = 349.^\circ70 \pm 0.^\circ56$, $\beta_{BV} = 35.^\circ72 \pm 2.^\circ06$, with the correlation coefficient equal to 0.82, as listed in the sixth row in Table 2.

The idea that the deflection of the secondary components of ISN neutrals from the inflow direction of the unperturbed ISN gas is in the plane defined by the velocity vector of the unperturbed ISN gas and the vector of ISMF results from heliospheric models including the ISMF and both excluding (e.g., Izmodenov et al. 2005) and including the interplanetary magnetic field (Pogorelov et al. 2008). The inflow direction of ISN H obtained by Lallement et al. (2010) is in fact a superposition of the inflow directions of the primary and secondary populations of ISN H, which are expected to be of comparable densities both in the heliospheric interface and within a few au from the Sun (Katushkina et al. 2015) where the signal observed by SWAN/*Solar and Heliospheric Observatory* and analyzed by Lallement et al. (2005) is formed. Thus, the ISN H direction is also expected to be coplanar with the plane determined by the Ribbon center and the ISN He inflow direction.

There are essentially two proposed physical mechanisms that create a Ribbon centered on the ISMF. The first of these concepts, proposed by McComas et al. (2009a) and first quantified by Heerikhuisen et al. (2010), involves the neutral solar wind (i.e., ENAs produced via charge exchange from solar wind protons), which travels out beyond the heliopause and forms a pickup ring after ionization. This mechanism requires that the pickup ring remains stable for long periods (months to years), allowing the pickup ring particles to undergo charge exchange and generate neutrals. Provided that the neutral particles are produced along the locus where the ISMF is roughly perpendicular to the radial direction ($B \cdot r \simeq 0$), some of these neutrals are directed back toward the Sun and can be observed by *IBEX*.

Several new pieces of evidence also suggest that the Ribbon center is in the direction of the ISMF. Schwadron et al. (2015b) used Voyager 1 observations beyond the heliopause to show that the observed magnetic field steadily rotates, which is consistent with the undraping of the ISMF as Voyager 1 moves further out toward the pristine ISMF. When the rotation is projected out into the pristine interstellar medium, it is found that the Voyager 1 field direction converges with the center of the *IBEX* Ribbon. This draping effect was further modeled by Zirnstein et al. (2015, 2016) and produces the Ribbon centers close to those observed by *IBEX*. These authors (Zirnstein et al. 2016) found that the direction to the Ribbon center as a function of energy changes relatively little and remains in the ***B*–*V*** plane.

The second piece of evidence indicating consistency between the center of the *IBEX* Ribbon and the ISMF is found from observations of TeV cosmic rays (Schwadron et al. 2014). In this case, the streaming of cosmic rays determined from TeV cosmic-ray anisotropies appears to roughly align with the direction of the ISMF determined from the Ribbon center.

The third piece of evidence that the *IBEX* Ribbon center is in the direction of the ISMF is the consistency of this direction with the interstellar field direction obtained from locally polarized starlight (Frisch et al. 2015). This implies that the ordering of the interstellar field persists over much larger spatial scales than that of the heliosphere.

5. SUMMARY AND CONCLUSIONS

We have analyzed observations of neutral He atoms collected by *IBEX*-Lo in energy channel 2 during ISN observation seasons 2010–2014 to estimate the Mach number, temperature, inflow direction and speed, and abundance of the WB discovered by Kubiak et al. (2014). We used data collected in the portion of Earth's orbit that had been excluded from the analysis of the ISN He parameters by Bzowski et al. (2015), Leonard et al. (2015), McComas et al. (2015a, 2015b), Möbius et al. (2015b), and Schwadron et al. (2015a). We assumed that the observed signal is a superposition of signals due to two Maxwell–Boltzmann populations of neutral He in front of the heliosphere: the primary ISN He population with the parameters known from Bzowski et al. (2015), and the WB population with the parameters we sought to fit. We used a parameter fitting method very similar to the method presented

by Swaczyna et al. (2015) and carried out simulations using the Warsaw Test Particle Model, presented by Sokół et al. (2015b), with the time-dependent ionization losses based on the helium ionization history from Sokół & Bzowski (2014).

We found that the WB parameter values obtained directly from the fitting procedure are highly correlated, similar to what was found by Bzowski et al. (2015) for the ISN He parameters, and that the minimum χ^2 value significantly exceeds the expected value. We also found that the fit results show some dependence on the data choice because, for some spin angles, the observed flux is sensitive to the drop in sensitivity of the *IBEX*-Lo instrument to low-energy He atoms, found by Galli et al. (2015) and Sokół et al. (2015a). This additional uncertainty mostly affects the inflow direction and temperature of the WB, and is larger than the formal parameter uncertainties obtained from the covariance matrix of the fit. With this additional uncertainty included, the WB inflow direction in the J2000 ecliptic coordinates is $\lambda_{\rm WB}$ $(251.57 \pm 0.50 \pm 0.9)^\circ$, $\beta_{\rm WB} = (11.95 \pm 0.30 \pm 0.6)^\circ$, $v_{\rm WB} = (11.28 \pm 0.48 \pm 0.7)$ km s^{-1}. The abundance relative to the primary ISN He is $\xi_{\rm WB} = (5.7 \pm 0.4 \pm 0.7) \cdot 10^{-2}$, the temperature is $T_{\rm WB} = (9.48 \pm 0.92 \pm 1.6) \cdot 10^3$ K, and the Mach number is $M_{\rm WB} = 1.97 \pm 0.04 \pm 0.05$: the correlations between the uncertainties that are shown as the first quantities in the arrays of two uncertainty values for each of the parameters are correlated with each other, and these correlations are described by Equations (2). The WB parameters obtained in the original derivation by Kubiak et al. (2014) marginally agree with that presently obtained (i.e., the error bars overlap), but the uncertainty obtained now is much smaller.

With the new, more precise direction of the WB and with the direction of inflow of ISN He obtained by Bzowski et al. (2014, 2015), Leonard et al. (2015), McComas et al. (2015a, 2015b), Schwadron et al. (2015a), and Wood et al. (2015) from *IBEX* and Ulysses observations, we find that these directions are coplanar within their respective uncertainty ranges. The plane that is fit to these four directions is in statistical agreement with a plane containing the directions of inflow of ISN He and the center of the *IBEX* Ribbon, as well as the plane fit to the directions of ISN He, ISN H from Lallement et al. (2010), as well as the plane fit to the directions of ISN He and WB. Thus, the results obtained in this paper for the WB, in the papers by Lallement et al. (2005) and Lallement et al. (2010) for ISN H, and by Funsten et al. (2013) for the Ribbon center, and by Bzowski et al. (2014, 2015), Leonard et al. (2015), McComas et al. (2015a, 2015b), Möbius et al. (2015a), Schwadron et al. (2015a), Wood et al. (2015), and Witte (2004) for ISN He, are consistent with the hypothesis that the WB is the secondary component of ISN He (Bzowski et al. 2012; Kubiak et al. 2014) and the hypothesis by McComas et al. (2009a), Schwadron et al. (2009), and Heerikhuisen et al. (2010) that the direction of the local ISMF coincides with the *IBEX* Ribbon center. This $\boldsymbol{B}$–$\boldsymbol{V}$ plane is given by its normal direction in the J2000 ecliptic coordinates $\lambda_{\rm BV} = 349.70^\circ \pm 0.^\circ56$, $\beta_{\rm BV} = 35.^\circ72 \pm 2.^\circ07$, with the correlation coefficient of 0.85.

The authors from SRC PAS acknowledge support from the Polish National Science Center grant 2012/06/M/ST9/00455.

REFERENCES

Baranov, V. B., Ermakov, M. K., & Lebedev, M. G. 1981, PAZh, 7, 372
Baranov, V. B., & Malama, Y. G. 1993, JGR, 98, 15157
Barnett, C. F., Hunter, H. T., Kirkpatrick, M. I., et al. 1990, Atomic Data for Fusion, Vol. ORNL-6086/V1 (Oak Ridge, TN: Oak Ridge National Laboratories)
Bochsler, P., Petersen, L., Möbius, E., et al. 2012, ApJS, 198, 13
Bzowski, M., Kubiak, M. A., Hłond, M., et al. 2014, A&A, 569, A8
Bzowski, M., Kubiak, M. A., Möbius, E., et al. 2012, ApJS, 198, 12
Bzowski, M., Sokół, J. M., Tokumaru, M., et al. 2013, in Cross-Calibration of Past and Present Far UV Spectra of Solar Objects and the Heliosphere, ed. R. Bonnet, E. Quémerais, & M. Snow (New York: Springer Science +Business Media), 67
Bzowski, M., Swaczyna, P., Kubiak, M., et al. 2015, ApJS, 220, 28
Frisch, P. C., Berdyugin, A., Piirola, V., et al. 2015, ApJ, 814, 112
Frisch, P. C., & Slavin, J. D. 2003, ApJ, 594, 844
Funsten, H. O., DeMajistre, R., Frisch, P. C., et al. 2013, ApJ, 776, 30
Fuselier, S. A., Allegrini, F., Bzowski, M., et al. 2014, ApJ, 784, 89
Fuselier, S. A., Bochsler, P., Chornay, D., et al. 2009, SSRv, 146, 117
Galli, A., Wurz, P., Fuselier, S., et al. 2014, ApJ, 796, 9
Galli, A., Wurz, P., Park, J., et al. 2015, ApJS, 220, 30
Heerikhuisen, J., Pogorelov, N. V., Zank, G. P., et al. 2010, ApJL, 708, L126
Izmodenov, V., Alexashov, D., & Myasnikov, A. 2005, A&A, 437, L35
Izmodenov, V. V., & Alexashov, D. B. 2015, ApJS, 220, 32
Katushkina, O. A., Izmodenov, V. V., Alexashov, D. B., Schwadron, N. A., & McComas, D. J. 2015, ApJS, 220, 33
Kubiak, M. A., Bzowski, M., Sokół, J. M., et al. 2013, A&A, 556, A39
Kubiak, M. A., Bzowski, M., Sokół, J. M., et al. 2014, ApJS, 213, 29
Lallement, R., Quémerais, E., Bertaux, J. L., et al. 2005, Sci, 307, 1447
Lallement, R., Quémerais, E., Koutroumpa, D., et al. 2010, in Twelfth Int. Solar Wind Conf. 1216, ed. M. Maksimovic et al. (Melville, NY: AIP), 555
Leonard, T. W., Möbius, E., Bzowski, M., et al. 2015, ApJ, 804, 42
McComas, D., Bzowski, M., Frisch, P., et al. 2015a, ApJ, 801, 28
McComas, D., Bzowski, M., Fuselier, S., et al. 2015b, ApJS, 220, 22
McComas, D. J., Alexashov, D., Bzowski, M., et al. 2012, Sci, 336, 1291
McComas, D. J., Allegrini, F., Bochsler, P., et al. 2009a, Sci, 326, 959
McComas, D. J., Allegrini, F., Bochsler, P., et al. 2009b, SSRv, 146, 11
McComas, D. J., Carrico, J. P., Hautamaki, B., et al. 2011, SpWea, 9, 11002
Möbius, E., Bochsler, P., Bzowski, M., et al. 2009a, Sci, 326, 969
Möbius, E., Bochsler, P., Heirtzler, D., et al. 2012, ApJS, 198, 11
Möbius, E., Bzowski, M., Fuselier, S. A., et al. 2015a, ApJS, 220, 24
Möbius, E., Bzowski, M., Fuselier, S. A., et al. 2015b, JPhCS, 577, 012019
Möbius, E., Kucharek, H., Clark, G., et al. 2009b, SSRv, 146, 149
Müller, H.-R., & Zank, G. P. 2004, JGR, 109, A07104
Olive, K., Agashe, K., Amster, C., et al. 2014, ChPhC, 38, 090001
Opher, M., Stone, E. C., Liewer, P. C., & Gombosi, T. 2006, AIP Conf. Ser. 858, Physics of the Inner Heliosheath, ed. J. Heerikhuisen et al. (Melville, NY: AIP), 45
Park, J., Kucharek, H., Möbius, E., et al. 2014, ApJ, 79, 97
Park, J., Kucharek, H., Möbius, E., et al. 2015, ApJS, 220, 34
Pogorelov, N. V., Borovikov, S. N., Zank, G. P., & Ogino, T. 2009, ApJ, 696, 1478
Pogorelov, N. V., Heerikhuisen, J., & Zank, G. P. 2008, ApJL, 675, L41
Rodríguez Moreno, D. F., Wurz, P., Saul, L., et al. 2013, A&A, 557, A125
Saul, L., Wurz, P., Möbius, E., et al. 2012, ApJS, 198, 14
Schwadron, N., Möbius, E., Leonard, T., et al. 2015a, ApJS, 220, 25
Schwadron, N. A., Adams, F. C., Christian, E. R., et al. 2014, Sci, 343, 988
Schwadron, N. A., Crew, G., Vanderspek, R., et al. 2009, SSRv, 146, 207
Schwadron, N. A., Moebius, E., Kucharek, H., et al. 2013, ApJ, 775, 86
Schwadron, N. A., Richardson, J. D., Burlaga, L. F., McComas, D. J., & Moebius, E. 2015b, ApJL, 813, L20
Sokół, J. M., & Bzowski, M. 2014, arXiv:1411.4826
Sokół, J. M., Bzowski, M., Kubiak, M., et al. 2015a, ApJS, 220, 29
Sokół, J. M., Kubiak, M., Bzowski, M., & Swaczyna, P. 2015b, ApJS, 220, 27
Swaczyna, P., Bzowski, M., Kubiak, M., et al. 2015, ApJS, 220, 26
Witte, M. 2004, A&A, 426, 835
Wood, B. E., Müller, H.-R., & Witte, M. 2015, ApJ, 801, 62
Wurz, P., Saul, L., Scheer, J. A., et al. 2008, JAP, 103, 054904
Zirnstein, E. J., Funsten, H. O., Heerikhuisen, J., & McComas, D. J. 2016, A&A, 586, A31
Zirnstein, E. J., Heerikhuisen, J., & McComas, D. J. 2015, ApJL, 804, L22